Microporous and Mesoporous Materials 174 (2013) 25–33

Contents lists available at SciVerse ScienceDirect

Microporous and Mesoporous Materials

journal homepage: www.elsevier.com/locate/micromeso

Nanoporous carbons from hydrothermally treated biomass as anode materials for lithium ion batteries

Ece Unur [a,*], Sergio Brutti [b], Stefania Panero [c], Bruno Scrosati [c]

[a] Department of Chemistry, Bursa Technical University, Osmangazi 16190, Bursa, Turkey
[b] Dipartimento di Scienze, Unviersità della Basilicata, V.le Ateneo Lucano 10, 85100 Potenza, Italy
[c] Dipartimento di Chimica, Università di Roma "Sapienza", Piazzale Aldo Moro 5, 00185 Rome, Italy

ARTICLE INFO

Article history:
Received 28 September 2012
Received in revised form 27 January 2013
Accepted 6 February 2013
Available online 4 March 2013

Keywords:
Lithium ion batteries
Biomass
Hydrothermal carbonization
Carbon anode

ABSTRACT

Biomass is transformed to carbon nanoparticles with surface-end groups called 'hydrochar' (**HC**) by an efficient and green hydrothermal carbonization (**HTC**) method. Three different approaches are used to introduce porosity to the **HC**: sole heat treatment, traditional potassium hydroxide (KOH) activation, and environmentally benign magnesium oxide (MgO) templating. All the resulting microporous materials are tested as Li-ion intercalation hosts in lithium cells by using an 1 M $LiPF_6$ in EC/DMC electrolyte solution. They all show stable reversible capacities at elevated current rates (1C), closely comparable to the maximum theoretical capacity of graphite. Among all the materials studied, the **HC-MA** with a surface area of 150 $m^2\ g^{-1}$ and obtained by MgO templating of the hydrochar shows the best cycling performance in lithium cell at room temperature (307 mAh g^{-1} at cycle 100 at 1C). The **HC-600** with the highest degree of aromaticity/order, lowest content of oxygen functional groups and surface area of 250 $m^2\ g^{-1}$, obtained by heating the hydrochar at 600 °C under inert atmosphere, shows the best power and overall performance with its ability to sustain high discharge/charge rates (1C, 2C, 5C, 10C, 20C). These electrochemical performances attained with materials of reasonable specific surface areas – obtained by green, low cost and practical strategies – can address the space limitations in Li-ion battery applications by improving volumetric energy densities.

1. Introduction

Depletion of fossil fuel resources and the global warming it brings about compels the search for alternative energy sources. The use of renewable energy sources, such as solar, wind, geothermal, hydrothermal and tidal eliminates greenhouse gas emissions and produces huge amounts of energy. The variable supply of energy and its deposition issues are the major barriers to utilization of these resources. Lithium ion batteries with high energy and power densities and long cycle lives come to aid at this point. Other than stationary energy storage, lithium ion batteries are anticipated to make a big impact on development of transportation technologies, such as hybrid electric vehicles (HEV), plug-in hybrid electric vehicles (PHEV) and electric vehicles (EV) [1–5].

The performance of the rechargeable lithium ion batteries is determined by the characteristics of the active materials employed in the electrodes. Carbonaceous materials have been the predominant anode materials for commercial rechargeable lithium ion batteries [6]. They show large variations in chemical properties, structure and morphology depending on the precursor and the method of preparation. Among them, highly ordered graphite exhibits long cycle life with a limited theoretical capacity of 372 mAh g^{-1} in its fully lithiated state (LiC_6) [7]. Amorphous microporous carbons offer higher capacities [7,8], but they suffer from large irreversible capacities in the first lithium insertion–deinsertion cycle [9–11]. Mechanisms responsible for irreversible capacity losses in amorphous carbon anodes are: formation of a solid-electrolyte interphase (SEI) as a result of electrolyte reduction on carbon surface at operating potentials close to that of Li/Li^+ and trapping of lithium ions in the carbon network due to interactions with oxygen containing surface functional groups or limited diffusion [12]. Both, the formation of SEI and the presence of functional groups on carbon surface, have twofold effects on the electrode performance. The hindrance of the diffusion of charge carriers between the anode and the electrolyte by the initially formed SEI and the presence of a layer of oxides prevent further electrolyte decomposition on anode [2,13,14]. The extent and thickness of the SEI and the electrochemical performance of the electrode can be controlled by tailoring the textural properties of the carbon [12] and its surface functional groups [14]. Several strategies to mitigate first cycle irreversible capacities have been reported in literature [15–17] and more importantly, this drawback is compensated by high mechanical stabilities of amorphous

* Corresponding author.
E-mail address: ece.unur@btu.edu.tr (E. Unur).

1387-1811/$ - see front matter © 2013 Elsevier Inc. All rights reserved.
http://dx.doi.org/10.1016/j.micromeso.2013.02.032

carbons to volumetric changes along lithium insertion–deinsertion cycles [18]. Therefore, nanostructured amorphous carbons with extensively developed network of interstitial spaces offer not only high capacity (energy) and high rate (power) anode materials with advanced cycling stabilities but also support materials for their mechanically weak inorganic competitors [7,18,19].

Considering the potential scale of application of high-energy and high-power battery technologies, the preparation of nanostructured anode materials from cost efficient renewable resources by sustainable and greener strategies is unavoidable [7]. Hydrothermal carbonization (**HTC**), which transforms aqueous dispersion of biomass to a thermochemically more stable, nanostructured carbonaceous material called 'hydrochar' (**HC**) at subcritical conditions, [20,21] offers a beneficial pretreatment method as it eliminates the costly and complicated drying steps, extends the choice of raw materials, and emits minimum amount of greenhouse gases while the exothermic reactions dominating the process renders it self sufficient after activation [22–24]. Porosity and high specific surface area, which improve the capacity [7], can be introduced into the hydrochar by potassium hydroxide (**KOH**) activation [25–27] or environmentally benign ceramic/magnesium oxide (**MgO**) templating [28]. The porosity can be tailored by controlling the activation/templating agent concentration and the treatment temperature [27,29]. The KOH is known to transforms into K_2CO_3 completely in C matrix as the temperature reaches 600 °C [25,30]. Nanoporous network that is rich in micropores is achieved by etching K_2CO_3 with acid solution. Increase in KOH concentration improves porosity and oxygen containing functional groups while an excessive dose may cause severe oxidation and collapse of C network [25,26,30]. Researchers have shown that the specific surface area and porosity of the hydrothermally treated D-glucosamine can be improved from 100 $m^2 g^{-1}$ (KOH/C (wt/wt) = 1) to 598 $m^2 g^{-1}$ (KOH/C = 4) by increasing KOH concentration [31]. In case of ceramic templating, coexistence of carbon and MgO prevent the agglomeration of both species and C precursor builds a nanoporous C films on MgO particles upon carbonization. Mesopores that inherit the size and morphology of MgO are formed upon dilute acid etching of MgO. Magnesium salts, such as magnesium acetate (MgAc) and magnesium citrate (MgCt), which complete their decomposition to MgO at lower temperatures than the carbon precursors [32], can be used as MgO resources and decomposing acetate and citrate groups would aid in the overall carbon yield while MgO can be recovered as magnesium salts by less hazardous acetic and citric acid solutions [28,29,32,33]. In their extensive comparative work on the effect of MgO/C precursor weight ratio on the structural properties and thus the capacitance of carbon electrodes, Morishita et al. showed that although maximum specific surface area is achieved at a ratio of 7/3, the best capacitive performance in powder mixed samples, including rate, is obtained at a ratio of 5/5 for MgAc/polyvinyl alcohol derived sample with mesopores whose diameters dominate at 5 nm [32].

In this contribution, an abundant agricultural biomass – hazelnut shells – are transformed to thermochemically more stable, nanostructured hydrochar by the efficient and green **HTC** method. Heat treatment under inert atmosphere, KOH activation and environmentally friendly MgO templating are utilized separately to enhance the textural properties, and thus the electrochemical performance of the hydrochar. The HTC of metal salts in the presence of carbohydrates is known to form spherical hydrophilic carbon shells incorporating metal ions, which yield hollow metal oxides upon calcination [34]. In this contribution, a similar phenomenon but a different approach is utilized to obtain porous carbons instead of hollow metal oxides. Hydrophilic carbon spheres incorporating metal ions obtained by the HTC of hazelnut shells in the presence of soluble metal salt (MgAc) are carbonized and then etched with acid solution to yield nanoporous carbons allowing the conduction of two separate processes; hydrothermal pretreatment and MgO templating, in one pot by saving energy and time. The Li ion storage performances of all the synthesized materials are studied comparatively in the view of their elemental compositions, surface functionalities, structural orders, textural properties and morphologies. To our knowledge, this is the first work in literature to report: anode materials derived from hydrothermally treated hazelnut shells, MgO templating of hydrochar, and HTC/MgO templating in one pot.

2. Experimental

Pulverized Merck potassium hydroxide (KOH) and Merck Magnesium Acetate tetrahydrate ($Mg(CH_3COO)_2{\cdot}4H_2O$; MgAc) were used as porogens. Eltra Thermostep Thermo-gravimetric Analyzer and alumina crucibles were used for sample preparation.

2.1. Sample preparation

Hazelnut shells ground with Herzog- HNM 100 disk mill were sifted with RETSCH vibratory sieve shaker to a powder with particle sizes smaller than 20 μm. Hazelnut shell powder (**HN**), citric acid and deionized water (18.2 MΩ cm^{-1} at 25 °C) were placed in a stainless steel autoclave (8:0.1:20, wt:wt:wt), heated to 250 °C and dwelled at that temperature for 7.5 h to obtain hydrochar (**HC**). HC obtained at subcritical conditions was dried in an oven prior to further use. **HC-600** was obtained by heating HC under a flow of argon at a rate of 10 °C min^{-1}–600 °C and dwelling at that temperature for 2 h. HC was mixed with pulverized KOH in a weight ratio of 1:4, heated under a flow of argon at a rate of 10 °C min^{-1}–600 °C, and dwelled at that temperature for 2 h. Sample was etched with hydrochloric acid solution and distilled water until its pH is neutral and dried in an oven. That sample was named **HC-KOH**. HN mixed with MgAc in 1:4 weight ratio (corresponding to HN/MgO weight ratio of almost 5/5) was placed in an agate jar and ball milled at 250 rpm for 75 min. The mixture was heated under a flow of argon at a rate of 10 °C min^{-1} to 600 °C, and dwelled at that temperature for 2 h. Sample was etched with citric acid solution and distilled water until its pH is neutral and dried in an oven. That sample was named **HN-MA**. HC mixed with MgAc in 1:4 weight ratio was placed in an agate jar and ball milled at 250 rpm for 75 min. The mixture was heated under a flow of argon at a rate of 10 °C min^{-1} to 600 °C, and dwelled at that temperature for 2 h. Sample was etched with citric acid solution and distilled water until its pH is neutral and dried in an oven. That sample was named **HC-MA**. HN, MgAc and deionized water (18.2 MΩ cm^{-1} at 25 °C) were placed in a stainless steel autoclave (1:4:5, wt:wt:wt), heated to 250 °C and dwelled at that temperature for 7.5 h. The product was washed with citric acid solution and distilled water until its pH is neutral and then heated under a flow of argon at a rate of 10 °C min^{-1} to 600 °C, and dwelled at that temperature for 2 h. The sample was named **HY-MO.**

2.2. Sample characterization

Relative weight losses of the samples were studied by Mettler Toledo (TGA/SDTA851) Thermogravimetric Analyzer (under N_2 flow) and Setaram Labsys TGA/DTA (under air). In order to observe relative weight loss due to carbonization, samples were heated under nitrogen to 950 °C at a 10 °C min^{-1} rate. In order to determine ash content, samples were heated under air to 980 °C at a 10 °C min^{-1} rate. Elemental analysis (C, H, N, S) of the samples were carried out on a LECO, CHNS-932 Elemental Analyser. In order to detect surface functional groups FT-IR (ATR) spectra of samples

were collected with Bruker IFS66/S FT-IR Spectrometer in the scanning range of 4000–400 cm^{-1}. The XRD experiments were carried out using a Rigaku X-ray Ultima + diffractometer equipped with a CuK_α source. The patterns were collected with steps of 0.04 and 2 counts. The Raman spectra were recorded on a LabRam HR MicroRaman Spectroscopy system (HORIBA Jobin Yvon) at an excitation wavelength of 632.8 nm. The Brunauer, Emmett & Teller (BET) and Density Functional Theory (DFT) methods were visited for calculations of the surface areas and pore size distributions, respectively. N_2 adsorption/desorption isotherms at 77 K were recorded by Quantachrome Corporation, Monosorb or Quantachrome Corporation, Autosorb-6. Prior to measurements samples were degassed at 200 °C for 10 h. Surface morphologies of the samples were studied by QUANTA 400F Field Emission SEM -Scanning Electron Microscope. Samples were sputtered with a 5 nm conductive coating (Au–Pd) prior to imaging.

2.3. Electrochemical characterizations

Slurries of carbonaceous materials were obtained by mixing active material (80%wt), Kynar 2801 PVDF-polyvinylidene fluoride (10%wt) and Timcal Super P Carbon (10%wt) in a minimum amount of tetrahydrofuran (THF). The slurries were cast onto thin copper foils (Cu), dried at room temperature and then pressed under 5 tons at 50 °C for 400 s by Carver Press (Auto Series). Electrode film was then cut into electrodes of 10 mm diameter: electrodes were dried under vacuum at 100 °C for 4 h in a BUCHI glass oven. Swagelock-like cells were assembled in an Ar-filled glovebox (MBraun) using lithium metal as the counter electrode, Merck Battery Grade LP30 (1 M lithiumhexafluorophosphate in ethylene carbonate:Dimethyl carbonate,1:1 w/w) as the electrolyte absorbed on Whatman™ separator and the carbon samples on Cu current collectors as the working electrodes. The cells were galvanostatically cycled at various C-rates in a 0.05–2.0 V range at room temperature by using a Maccor Series 4000 Battery Test System. The specific capacity values reported in this paper refer to the active material mass only.

3. Results and discussion

3.1. Characterizations of the carbonaceous samples

Potassium hydroxide (KOH) is known as an effective activating agent for both ordered and disordered carbons as its reactions with carbon starts at temperatures as low as 400 °C and all the KOH gets converted to potassium carbonates (K_2CO_3) at 600 °C [25,30]. Magnesium acetate, which is used as an MgO template precursor, starts its major decomposition at 325 °C and completely converts to MgO as the temperature reaches 450 °C, as shown in Fig. 1. (The presence of MgO in the carbon matrix after carbonization is confirmed by XRD results. Supplementary Material, Fig. S1.) Nanoporous networks are obtained upon removal of K_2CO_3 or MgO from the carbon matrices by acid wash. Hazelnut shells are composed of 30% amorphous hemicellulose, 27% crystalline cellulose and 43% aromatic lignin [35]. The thermal decomposition of lignin takes place over the entire pyrolysis range while hemicellulose decomposes in the 200–320 °C region and cellulose in the 200–400 °C with the main decomposition taking place at 300–600 °C [36,37]. Higher temperatures result in complete decomposition of lignin, and thus the collapse of the structure. Therefore, 600 °C which assures complete carbonization of cellulosic parts while preserving part of aromatic structure and ensuring full performance of activating and templating agents was set as the pyrolysis temperature in this work [33].

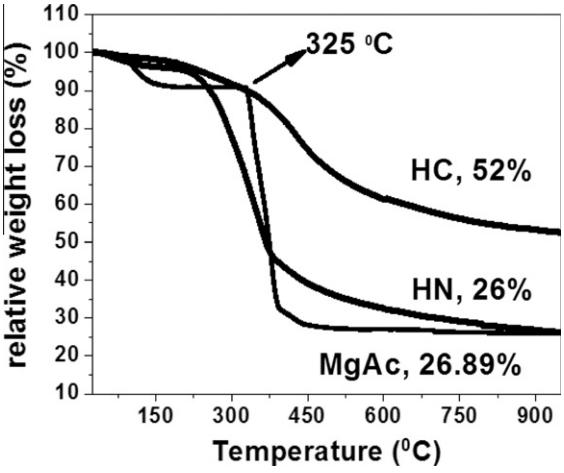

Fig. 1. Thermal characterization of HN, HC and MgAc. (The samples were heated to 950 °C at a 10 °C min^{-1} rate under N_2.)

The thermal stabilities of the samples are studied by thermogravimetric analyses. As seen in Fig. 1, HN starts to decompose at 200 °C and about 51% of the weight, associated with the decomposition of mostly cellulosic and partly lignin content, is lost as the temperature reaches 400 °C, the final yield being 26% at 950 °C. The major decomposition taking place at higher temperatures (330–600 °C) and twice as much yield (52%) indicates thermochemically more stable nature of hydrochar (**HC**) due to decomposition of cellulosic content during hydrothermal carbonization (**HTC**). Further heat treatment, KOH activation, and MgO templating result in improved thermal stabilities of the samples since they all loose only 20–30% weight as they are heated to 950 °C (Supplementary Material, Fig. S2).

The high oxygen content (39.17 wt.%) of biomass, prone to surface functionality, is confirmed by the elemental analysis results (Table 1). High concentrations of oxygen functional groups are not favored in battery applications, since they form a very extensive solid-electrolyte interphase (SEI) which increases irreversible capacity. However, a thin SEI formed on mildly oxidized carbon surface is favored as it prevents further decomposition of electrolyte on carbon anode [13,14]. While **HTC** and **HTC** followed by KOH activation or MgO templating increase C content to values of 65–71 wt.%, they maintain O content at around 19–31 wt.%. The O content of HC-KOH (31 wt.%), even higher than its precursors HC's (23 wt.%), confirms our FTIR results and the finding of other researchers that KOH favors regeneration of oxygen containing surface functional groups [26]. The sole heat treatment of **HC** at 600 °C results in the maximum C content (78 wt.%) and minimum O content (9 wt.%) of all the samples, indicating the greater extent of carbonization and disruption of surface functional groups, respectively.

Plot of atomic H/C ratios against the atomic O/C ratios (aka. the van Krevelen Diagram) displays reactions related to carbonization [38,39]. Almost linear evolution of atomic ratios of the samples on the van Krevelen Diagram (Fig. 2) indicates the increase in carbonaceous nature and aromaticity mostly by dehydration during hydrothermal and thermal treatments. Slight shifts from linearity observed for HN-MA, HC-MA and HY-MO are attributed to side reactions, such as decarboxylation. The major shift from linearity, observed for HC-KOH, is associated with the oxidation emanating from chemical activation. HC-600 with the highest C content and lowest O content has the most aromatic character of all the materials.

FTIR analyses were conducted to study surface functional groups of the carbonaceous samples (Supplementary Material,

Table 1
Elemental compositions and textural properties of the carbonaceous samples.

Sample	Elemental composition, wt.%				Atomic ratios		Textural properties	
	C	H	N	O[a]	H/C	O/C	S_{BET}[b] $m^2 g^{-1}$	V_{pore}[c] $cm^3 g^{-1}$
HN	47.1	5.9	0.6	39.2	1.5	0.6	30	0.04
HC	65.8	4.7	1.0	23.3	0.9	0.3	60	0.05
HC-600	78.4	3.0	1.0	9.0	0.5	0.1	250	0.17
HC-KOH	64.5	2.8	0.4	31.0	0.5	0.4	1700	0.79
HN-MA	66.5	3.4	0.6	23.0	0.6	0.3	44	0.04
HC-MA	70.2	3.2	0.5	19.0	0.5	0.2	150	0.12
HY-MO	70.9	3.1	0.9	22.2	0.5	0.2	320	0.21

[a] By difference, O% = 100 − %(C + H + N + S + Ash).
[b] Specific surface area by BET method.
[c] Specific pore volume by DFT method.

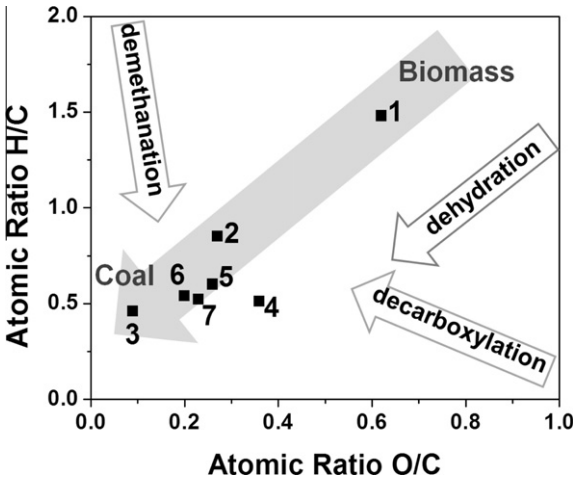

Fig. 2. Evolution of the elemental compositions of the samples by means of Van Krevelen diagram. (1) HN, (2) HC, (3) HC-600, (4) HC-KOH, (5) HN-MA, (6) HC-MA, and (7) HY-MO.

Fig. S3). The bands and peaks of HN are preserved in HC: the band associated with O–H stretching vibrations of hydroxyl groups of cellulose at 3300 cm^{-1}, the band attributed to aliphatic C–H stretching vibrations of cellulosic structure at 3000–2000 cm^{-1}, the peak resulting from C=O stretching vibrations of carbonyl/carboxyl groups at about 1700 cm^{-1}, the peaks of C=C stretching vibrations of alkenes and aromatic rings at about 1607 cm^{-1} and 1516 cm^{-1}, and most importantly, the characteristic peak of cellulose at 1014 cm^{-1} resulting from C–O stretching vibrations of alcohols and phenols [20]. The symmetric and asymmetric C=C stretching vibration peaks of aromatic rings at 1590 cm^{-1} and 1380 cm^{-1}, and the peaks in the 900–750 cm^{-1} region related to aromatic C–H bendings for HC-600 confirms the increasing degree of aromatization. The lack of O–H stretching vibrations of hydroxyl at 3300 cm^{-1} and decreasing intensity of C=O peak of carbonyl groups at 1700 cm^{-1}, in HC-600 spectrum, indicates the depletion of oxygen containing surface functional groups by heat treatment. In the case of HC-KOH, the depletion of asymmetric C=C aromatic ring stretches in the 1500–1300 cm^{-1} region and C–H bending peaks in the 900–750 cm^{-1} region, and appearance of C–O stretching vibration peak of alcohol an phenols at 1074 cm^{-1} can be associated with the regeneration of some oxygen functional groups at the expense of aromaticity by KOH activation. The HN-MA, HC-MA and HY-MO show very similar FTIR spectra with HC-600 with the dominating peaks associated with the following; asymmetric and symmetric C=C stretching vibrations of aromatic rings (2 peaks in the 1600–1400 cm^{-1} region), C–O stretching vibration peak of ethers and esters at 1200 cm^{-1} and aromatic C–H bending peaks at 900–750 cm^{-1} region. Heat treatment under inert atmosphere, by destroying oxygen containing functional groups and increasing aromaticity allows the control of surface functionality and thus the SEI thickness.

The pyrolysis temperature is expected to play a major role in the order of the material. Higher temperatures with higher energies break the links between adjacent planes and favor their parallel alignment. While disorder is known to increase capacity by inserting more lithium ions, some order is required to ensure that the ions are retrievable and the process is reversible. The structural order of the carbon samples are examined by XRD (Fig. 3) and Raman analyses (Supplementary Material, Fig. S4). The XRD diffraction patterns of all samples show broad peaks at 2θ value of 25° attributed to the (002) interlayer reflections among irregularly oriented polycyclic aromatic C sheets of amorphous carbon [40,41]. The very weak and broad reflections centered at 2θ value of 45°, observed for the samples treated at 600 °C, corresponds to (100) in-plane scattering and indicates an increasing degree of order with thermal treatment in agreement with the D and G bands associated with order and observed near 1360 and 1590 cm^{-1}, respectively, in the spectra of all the samples other than HN and HC.

SEM images (Fig. 4), BET specific surface areas and pore volumes recorded (Table 1) provide insight about the textural and morphological properties of the carbon samples. HN, with a very smooth surface, dissociates into smaller organic units and then reconstitutes into bicontinuous network of agglomerated nanostructures during hydrothermal treatment (**HC**) and the increases in specific surface area to 60 $m^2 g^{-1}$ can be attributed to increase in surface roughness only as the increase in pore volume is insignificant. The heat treatment at 600 °C transforms the agglomerates

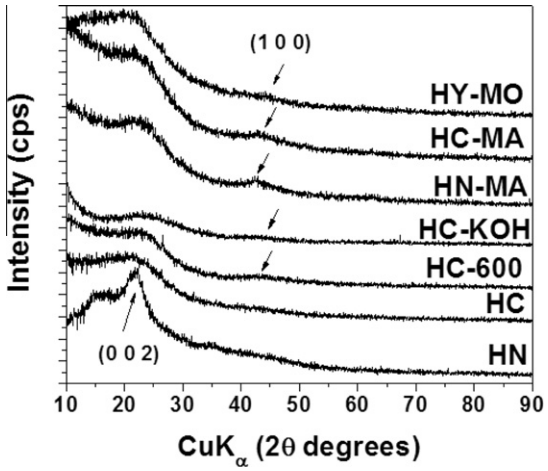

Fig. 3. XRD patterns of the resultant carbonaceous samples; HN, HC, HC-600, HC-KOH, HN-MA, HC-MA and HY-MO.

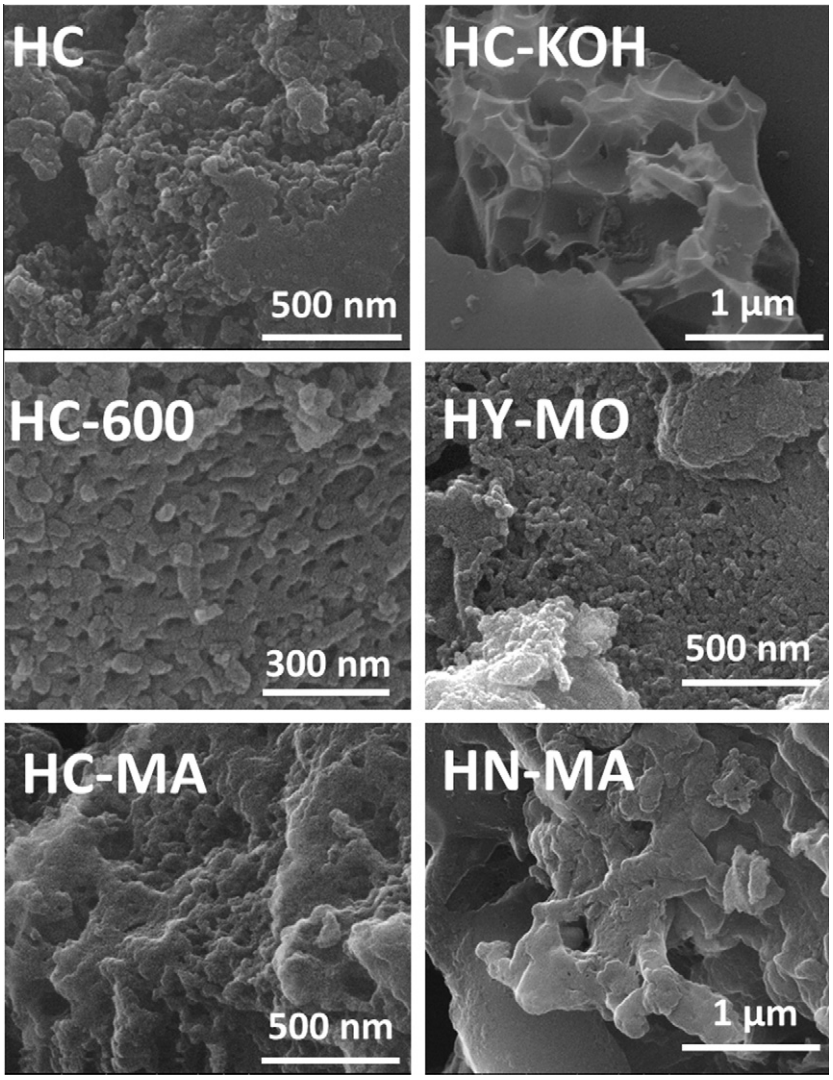

Fig. 4. SEM images of carbonaceous materials.

of nanostructures (**HC**) into a compact network of quasi-spheres in the nm range with interstitial spaces (**HC-600**) increasing the specific surface area from 60 $m^2 g^{-1}$ to 250 $m^2 g^{-1}$ and specific pore volume more than 3 times to 0.17 $cm^{-3} g^{-1}$. The more open pore structure with a specific pore volume of 0.79 $cm^{-3} g^{-1}$ and high specific surface area of 1700 $m^2 g^{-1}$ achieved with **HC-KOH** can be explained by the stretching of the lattice due to conversion of carbons to higher volume carbonates upon KOH activation and the spaces left behind after their removal by acid solution [25,26,30]. HN-MA obtained by MgO templating of **HN** results in increase of specific surface area while the specific pore volume stays the same indicating the increase in surface roughness but porosity in accordance with SEM images of HN-MA displaying sponge-like nanostructural elements among smoother sections. On the other hand, HC-MA obtained by MgO templating of **HC** (hydrochar) displays a sponge-like morphology with improved specific pore volume (0.12 $cm^{-3} g^{-1}$) and surface area (150 $m^2 g^{-1}$), compared to HN-MA, reflecting the positive effect of hydrothermal pretreatment on textural properties. Better textural properties of **HC-600** compared to **HC-MA** shows that interstitial spaces achieved by hydrothermal treatment are probably coagulated by carbonizing acetate groups of MgAc and an effective interaction between the MgO-template and the C-network could not be achieved. HY-MO, prepared by the hydrothermal treatment of HN in the presence of MgO followed by thermal treatment at 600 °C, shows morphological properties very similar to that of **HC-600** and higher specific surface area and pore volumes of 320 $m^2 g^{-1}$ and 0.21 $cm^{-3} g^{-1}$, respectively, indicating the effective templating achieved by hydrothermal pretreatment. Metal ions from MgAc incorporated in hydrophilic carbon shells during hydrothermal treatment alleviates the coalescence of both species and increases the amount of interstitial spaces which are widened to form micro and mesopores upon further heat treatment in case of HY-MO.

DFT pore size distributions of the samples are shown in Fig. 5. The HN and HC show similar pore characteristics since HN offers very little porosity and hydrothermal treatment has no affect on porosity but surface roughness. The MgO templating of very smooth HN does not increase pore volume but increases the concentration of micropores in the carbon matrix. All the samples derived from HC show narrow pore size distributions and they are dominated by micropores of 1–1.9 nm porewidths which are accompanied by lower concentration of mesopores of 2–3.3 nm porewidths. Significantly higher micropore volumes suggest that further heat treatment, KOH activation and MgO templating are responsible for the formation of micropores. On the other hand, mesopores of 2–3.3 nm porewidths observed only for HC derived samples (i.e. HN-MA vs. HC-MA), suggests that they are formed

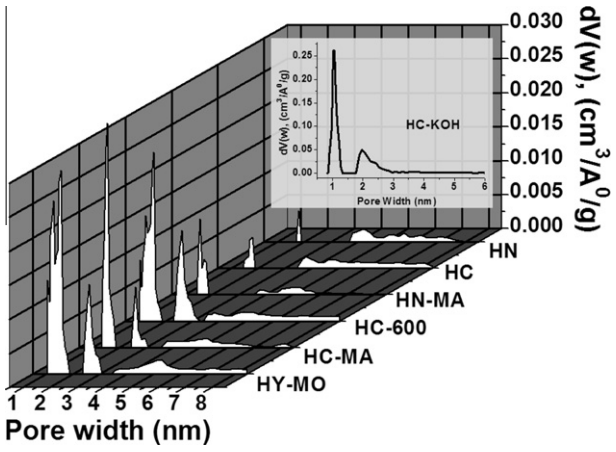

Fig. 5. DFT pore size distributions of the resultant carbonaceous samples; HN, HC, HN-MA, HC-600, HC-MA, HY-MO and HC-KOH.

by widening of the preexisting micropores in HC matrix. The smaller pore diameters (~2 nm) compared to the ones reported in literature (~5 nm) for MgAc templated carbons [32] can be attributed to smaller size of MgAc obtained by ball-milling prior to carbonization in case of HN-MA and HC-MA and to metal ion/C composite formation due to extreme conditions of hydrothermal treatment in case of HY-MO. The specific surface area, morphology, pore volume and pore size distribution data, discussed above, prove that the pore numbers and sizes can be controlled by the choice of precursor and treatment method. The samples with extensively developed micro and meso porosities which guarantee facile storage and diffusion of Li ions, respectively, and offer sufficient surfaces for effective electrode/electrolyte interactions do promise as high capacity Li ion inserting anode materials [7].

3.2. Electrochemical characterization of carbonaceous samples

In order to achieve high overall electrochemical performances; samples must accommodate large amount of Li ions to increase capacity (high concentration of micropores and high specific surface area) and offer free transport pathways to Li ions to attain high rates/current densities (high concentration of mesopores). The galvanostatic cycling characteristics of the samples are summarized in Table 2 and displayed in Fig. 6. The first cycle discharge/charge capacities are all greater and the capacities retained after 100 cycles are all comparable to the maximum theoretical capacity that can be obtained from perfectly graphitic structures (372 mAh g^{-1}) [7] even at high rates (1C = 372 mA g^{-1}). More than that, the electrochemical performances of all our hydrothermally pretreated **pure-carbon** anodes (Table 2) are comparable to or better than the performance reported for the carbon/silicon nanocomposites (repoted as: 1st cycle discharge and charge capacities of ~1200 mAh g^{-1} and ~500 mAh g^{-1}, respectively and reversible capacity of 460 mAh g^{-1} at 300 mA g^{-1} rate over 20 cycles) obtained by hydrothermal carbonization of glucose in the presence of silicon nanoparticles which have a very high theoretical capacity of 4200 mAh g^{-1} [19].

The HC-KOH with its extensively improved micro porosity and high specific surface area, shows very high first cycle discharge (2558.75 mAh g^{-1}) and charge capacities (701.79 mAh g^{-1}) at 1C-rate. However, the improved capacity is offset by large irreversible capacity (CE 27.43%, 1856.96 mAh g^{-1}) arising from uncontrollable SEI formation on the large surface as a result of high content of oxygen functional groups as confirmed by the FTIR data and much lower concentration of mesopores compared to micropores resulting in entrapment of large accounts of Li ions in micropores. Coulombic efficiency improves as the cycling progresses and reaches 98.88% at 100th cycle with a discharge capacity of 300 mAh g^{-1}.

The use of gentler chemical agent, MgO, enables the development of more controlled textural properties in an environmentally friendly manner. MgO templating of HC gives a porous nanostructured aromatic network with a controlled specific surface area (150 m^2 g^{-1}) and limited surface functional groups. Even though, lower first cycle discharge (1270 mAh g^{-1}) and charge (510.96 mAh g^{-1}) capacities are recorded for HC-MA, the coulombic efficiency improves to 40.23% with an only 759.04 mAh g^{-1} loss of capacity due to less extensive SEI formation and comparable micro and meso pore volumes improving diffusion of ions in the matrix. The 100th cycle discharge capacity of HC-MA (307.24 mAh g^{-1}) also comparable to the HC-KOH's proves that milder carbonization processes are also able to give promising carbon materials for Li-cells.

Comparison of performances of HN-MA and HC-MA reflects the contribution of HTC pretreatment on the performance of the materials. The low capacities observed for HN-MA (100th cycle discharge capacity of 138.83 mAh g^{-1}, Supplementary Material, Fig. S5), which wasn't put through hydrothermal pretreatment, can be attributed to poorly developed nanoarchitecture and low specific surface area (44 m^2 g^{-1}) which do not offer enough sites for Li ion accommodation.

Table 2
Summary of the galvanostatic cycling characteristics of the samples at 1C (1 M $LiPF_6$ in EC/DMC).

Sample	Cycle number	Discharge capacity[a]	Charge capacity[a]	Irreversible capacity[a]	%CE[b]
HC-KOH	1	2558.75	701.79	1856.96	27.43
	50	**345.16**	**339.49**	**5.67**	**98.36**
	100	300.42	297.05	3.37	98.88
HN-MA	1	514.06	149.10	364.95	29.01
	50	**135.29**	**133.35**	**1.94**	**98.56**
	100	138.83	136.71	2.12	98.47
HC-MA	1	1270	510.96	759.04	40.23
	50	**353.4**	**350.49**	**2.91**	**99.18**
	100	307.24	305.26	1.98	99.35
HY-MO	1	1050.65	375.92	674.73	35.78
	50	**259.13**	**255.33**	**3.80**	**98.53**
	100	247.23	246.80	0.44	99.82
HC-600	1	1331.19	607.53	723.66	45.64
	50	**318.67**	**315.03**	**3.64**	**98.86**
	100	291.54	289.64	1.91	99.35

[a] mAh g^{-1}.
[b] %CE = 100 × (charge capacity/discharge capacity).

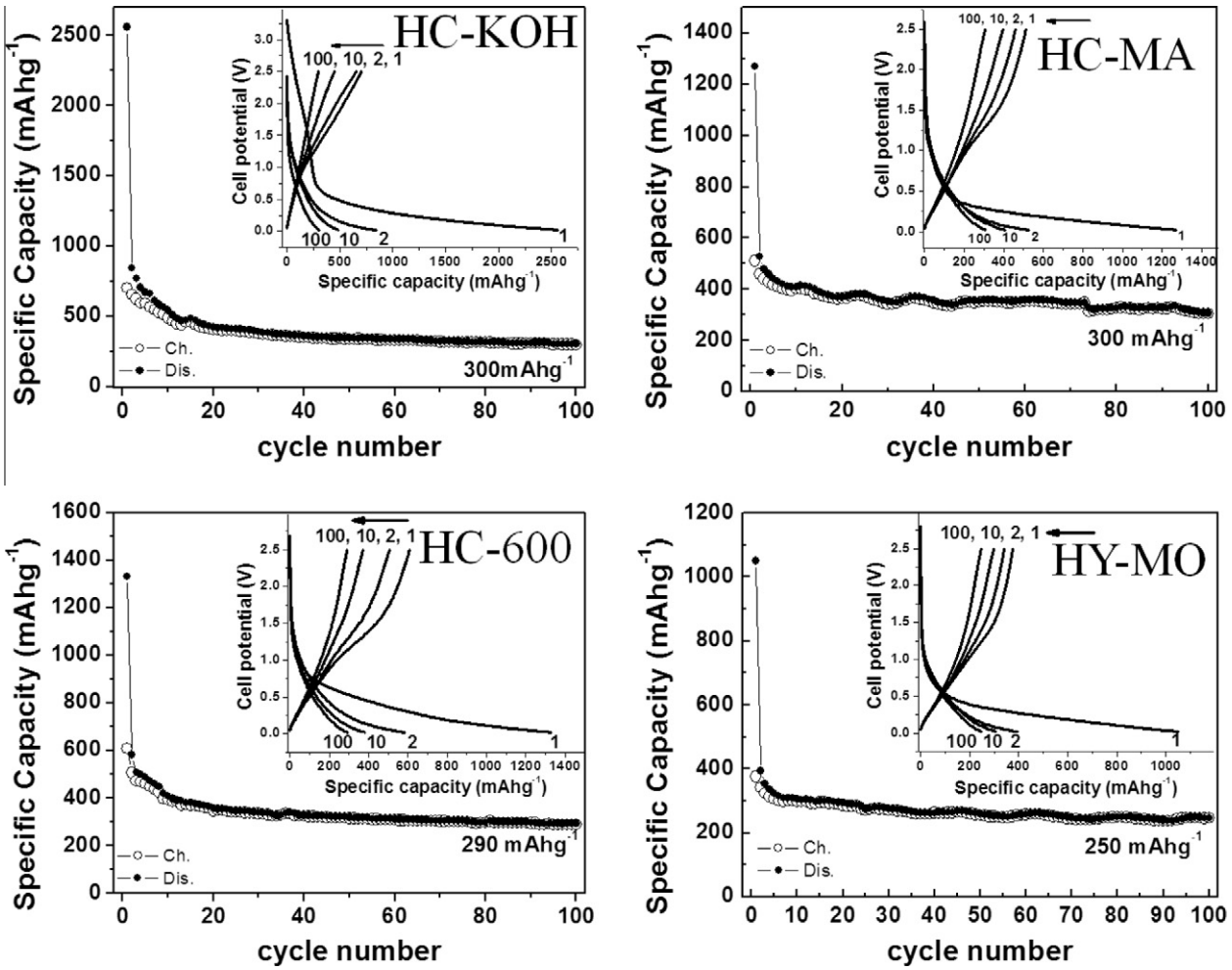

Fig. 6. Galvanostatic cycling performances of the samples' electrodes cycled at a 1C-rate (372 mA g^{-1}) between voltage limits of 0.05–2 V in 1 M $LiPF_6$ in EC/DMC solution. Insets: Voltage profiles of the samples' electrodes at 1st, 2nd, 10th and 100th cycles.

The proven contribution of HTC and MgO templating on the materials' properties, reflect to the electrochemical performance of HY-MO which was obtained by simultaneous HTC pretreatment and MgO templating of HN. As expected, HY-MO with higher surface area (320 m^2 g^{-1}) shows a performance comparable to HC-MA's with 100th cycle discharge capacity of 247.23 mAh g^{-1} at 1C rate confirming that a material of similar performance is obtained by a less laborious method.

As more controlled textural properties are shown to offer high capacities, we investigated the performance of HC-600 which was obtained by successive hydrothermal and thermal treatments of HN precursor without any additional chemical agents. To our surprise, the HC-600 obtained by this very practical approach shows electrochemical performances just as good as the other materials presented in this contribution with a high 100th cycle discharge capacity of 291.54 mAh g^{-1} at 1C. The high first cycle discharge (1331.19 mAh g^{-1}) and charge (607.53 mAh g^{-1}) capacities of HC-600 are accompanied by the highest first cycle coulombic efficiency recorded of all the samples (45.64% CE). This lowest irreversible capacity loss recorded in the first cycle arises from the controlled SEI formation due to minimum amount of oxygen functional groups present (9 wt.% O) on the optimum surface area (250 m^2 g^{-1}) of HC-600.

Galvanostatic cycling carried out at high rates (1, 2, 5, 10 and 20C) allows comparison of power performances of materials (Fig. 7). The stability of the capacities and the ability of the carbons to sustain high-rate discharge/charge are noteworthy. The discharge capacities for HC-KOH, HC-MA, and HY-MO are 61 mAh g^{-1}, 68 mAh g^{-1} and 68 mAh g^{-1}, respectively, at 100th cycle. As shown in Fig. 7, the HC-600 gives a discharge capacity of 370 mAh g^{-1} after 20 cycles of discharge/charge at 1C rate, 300 mAh g^{-1} after 20 cycles at 2C rate, 230 mAh g^{-1} after 20 cycles at 5C rate, 170 mAh g^{-1} after 20 cycles at 10C rate, and 113 mAh g^{-1} after 20 cycles at 20C rate. Almost twice as much capacity observed for HC-600 at the end of 100 cycles high rate discharge/charge performance compared to other samples, points to better rate capability, and thus better specific power performance of HC-600 as a result of higher structural order and well developed network of micro- and mesopores which all together allow fast transport of Li ions by offering free pathways.

The HC-600 has the highest C (78%) and lowest O (9%) content of all the samples, resulting in the highest order of structure and aromaticity, lowest amount of oxygen containing surface functional groups, and thus the lowest amount of first cycle irreversible capacity due to controlled formation of SEI. These unique properties, together with micropores to accommodate high amounts of Li ions, ordered and well developed mesopores to enhance ion transport, and the specific surface area (250 mAh g^{-1}) allowing optimum interaction between the electrolyte and the sample are responsible for the improved capacity and rate performance of HC-600.

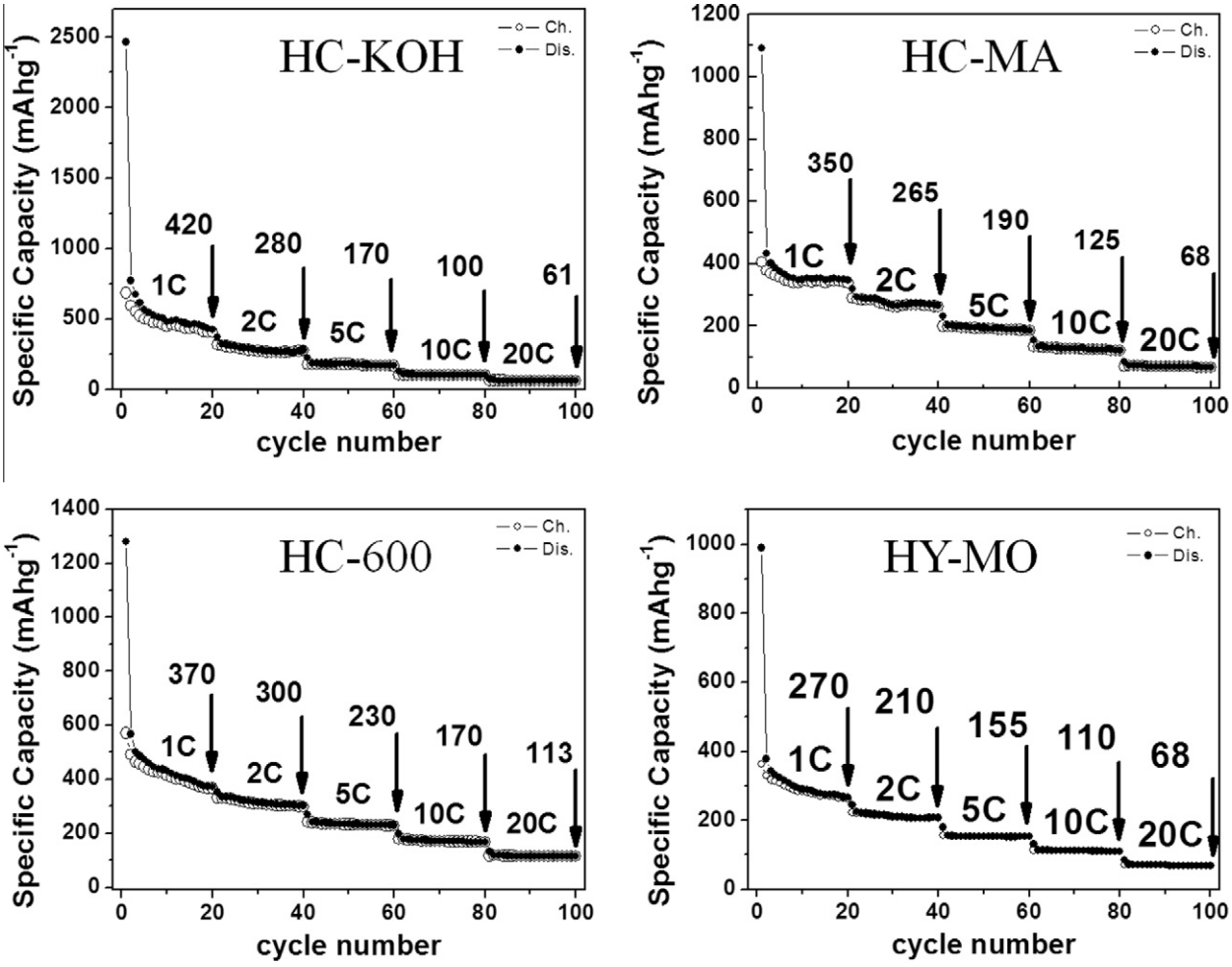

Fig. 7. Galvanostatic cycling and rate performances of the samples' electrodes. (1C = 372 mA g^{-1}, between voltage limits of 0.02–2.5 V in 1 M $LiPF_6$ in EC/DMC solution. 20 cycles at each rate; 1C, 2C, 5C, 10C, and 20C.) The numbers on the plots display the discharge capacities in mAh g^{-1} at every 20th cycles.

4. Conclusions

An abundant agricultural biomass – hazelnut shells – [35] were transformed to carbon nanostructures with improved thermochemical stabilities by the efficient and green HTC method. The KOH activation, MgO templating, and a sole heat treatment under inert atmosphere were utilized to improve textural and morphological properties, control surface chemistry and further improve thermal stability. The **HC-600**, obtained by successive hydrothermal and thermal treatments of HN precursor without additional chemical agents offer; minimum surface functionality, maximum aromaticity and structural order, optimum specific surface area, and well developed micro- and mesoporous network, and proves ideal as high capacity (energy) and high rate capability (power) anode material for lithium ion batteries. In addition the HTC pretreatment stands out as a practical method of improving structural order without the need for additional chemical agents. The green, low cost and practical strategies used to achieve anode materials of excellent overall performances in this contribution can easily be scaled up for industrial applications. The promising electrochemical performances attained with materials of reasonable specific surface areas compared to the traditional activated carbons' addresses the space limitations associated with Li-ion batteries by offering high volumetric energy densities.

Acknowledgements

Authors are grateful to Bursa Cement Factory Co., Inc. for allowing the use of their facilities for the preparation of the samples. Authors extend their sincere gratitude to the Middle East Technical University Central Laboratory for their support in characterization experiments and Dr.Angela De Bonis from University of Basilicata (Potenza) for her support with Raman Spectroscopy. Last but not least, authors would like to thank Tekno-Last Ltd., Inc. for financially supporting this project.

Appendix A. Supplementary data

Supplementary data associated with this article can be found, in the online version, at http://dx.doi.org/10.1016/j.micromeso.2013.02.032.

References

[1] B. Scrosati, J. Garche, J. Power Sources 195 (2010) 2419–2430.
[2] A. Manthiram, J. Phys. Chem. Lett. 2 (2011) 176–184.
[3] J.B. Goodenough, Y. Kim, Chem. Mater. 22 (2010) 587–603.
[4] B. Scrosati, W.A. van Schalwijck, Introduction, Kluwer Academic/Plenum Publishers, New York, 2002.
[5] M. Armand, J.M. Tarascon, Nature 451 (2008) 652–657.

[6] M. Winter, J.O. Besenhard, M.E. Spahr, P. Novak, Adv. Mater. 10 (1998) 725–763.
[7] L. Ji, Z. Lin, M. Alcoutlabi, X. Zhang, Energy Environ. Sci. 4 (2011) 2682–2699.
[8] F. Bonino, S. Brutti, P. Reale, B. Scrosati, L. Gherghel, J. Wu, K. Mullen, Adv. Mater. 17 (2005) 743–746.
[9] F. Cheng, Z. Tao, J. Liang, J. Chen, Chem. Mater. 20 (2008) 667–681.
[10] F. Bonino, S. Brutti, M. Piana, B. Scrosati, L. Brambilla, G. Fustella, C. Castiglioni, G. Zerbi, D. Zane, T. Renouard, C. Mathis, J. Electrochem. Soc. 152 (2005) A2023–A2029.
[11] F. Bonino, S. Brutti, M. Piana, S. Natale, B. Scrosati, L. Gherghel, K. Müllen, Electrochim. Acta 51 (2006) 3407–3412.
[12] T.P. Kumar, T.S.D. Kumari, A.M. Stephan, J. Indian Inst. Sci. 89 (2009) 393–424.
[13] C. Menachem, Y. Wang, J. Flowers, E. Peled, S.G. Greenbaum, J. Power Sources 76 (1998) 180–185.
[14] Y.J. Kim, H.J. Lee, S.W. Lee, B.W. Cho, C.R. Park, Carbon 43 (2005) 163–169.
[15] S.S. Zhang, J. Power Sources 162 (2006) 1379–1394.
[16] I. Isaev, G. Salitra, A. Soffer, Y.S. Cohen, D. Aurbach, J. Fischer, J. Power Sources 119–121 (2003) 28–33.
[17] M. Gaberscek, M. Bele, J. Drofenik, R. Dominko, S. Pejovnik, Electrochem. Solid St. 3 (2000) 171–173.
[18] B.-S. Lee, S.-B. Son, K.-M. Park, W.-R. Yu, K.-H. Oh, S.H. Lee, J. Power Sources 199 (2012) 53–60.
[19] R.D. Cakan, M.M. Titirici, M. Antonietti, G. Cui, J. Maier, Y.-S. Hu, Chem. Commun. (2008) 3759–3761.
[20] M. Sevilla, H.A. Macia-Agullo, A.B. Fuertes, Biomass Bioenergy 35 (2011) 3152–3159.
[21] X. Sun, Y. Li, Angew. Chem. Int. Ed. 43 (2004) 597–601.
[22] A. Funke, F. Ziegler, Bioprod. Bioref. 4 (2010) 160–177.
[23] S.K. Hoekman, A. Broch, C. Robbins, Energy Fuel 25 (2011) 1802–1810.
[24] M. Titirici, T. Arne, M. Antonietti, New J. Chem. 31 (2007) 787–789.
[25] M.A. Lillo-Rodenas, D. Cazorla-Amoros, A. Linares-Solano, Carbon 41 (2003) 267–275.
[26] R.L. Tseng, S.K. Tseng, F.C. Wu, C.C. Hu, C.C. Wang, J. Chin. Inst. Chem. Eng. 39 (2008) 37–47.
[27] J. Romanos, M. Beckner, T. Rash, L. Firlej, B. Kuchta, P. Yu, G. Suppes, C. Wexler, P. Pfeifer, Nanotechnology 23 (2012) 015401–015407.
[28] M. Inagaki, S. Kobayashi, F. Kojin, N. Tanaka, T. Morishita, B. Tryba, Carbon 42 (2004) 3153–3158.
[29] T. Morishita, T. Tsumura, M. Toyoda, J. Przepiorski, A.W. Morawski, H. Konno, M. Inagaki, Carbon 48 (2010) 2690–2707.
[30] E. Raymundo-Pinero, P. Azais, T. Cacciaguerra, D. Cazorla-Amoros, A. Linares-Solano, F. Beguin, Carbon 43 (2005) 786–795.
[31] L. Zhao, L. Fan, M. Zhou, H. Guan, S. Qiao, M. Antonietti, M. Titirici, Adv. Mater. 22 (2010) 5202–5206.
[32] T. Morishita, Y. Soneda, T. Tsumura, M. Inagaki, Carbon 44 (2006) 2360–2367.
[33] E. Unur, Micropor. Mesopor. Mater. 168 (2013) 92–101.
[34] M.M. Titirici, M. Antonietti, A. Thomas, Chem. Mater. 18 (2006) 3808–3812.
[35] A. Demirbas, Energy Sources 24 (2002) 215–221.
[36] D.K. Seo, S.S. Park, J. Hwang, T.-U. Yu, J. Anal. Appl. Pyrol. 89 (2010) 66–73.
[37] L. Yu, C. Falco, J. Weber, R.J. White, J.Y. Howe, M.M. Titirici, Langmuir 28 (2012).
[38] M. Sevilla, A.B. Fuertes, Carbon 47 (2009) 2281–2289.
[39] J.H. Gross, Mass Spectrometry: A textbook, Springer, Heidelberg.
[40] M.M. Titirici, A. Thomas, M. Antonietti, Adv. Funct. Mater. 17 (2007).
[41] R.J. White, M. Antonietti, M. Titirici, J. Mater. Chem. 19 (2009) 8645–8650.